RSC Advances

PAPER

View Article Online
View Journal | View Issue

Cite this: *RSC Adv.*, 2025, **15**, 33991

Portable ratiometric fluorescence sensor based on CuNCs@EuMOFs for visual detection of Hg(II) in water samples

Jiaxu Tian,[a] Chenfeng Wang,[a] *[a] Yueyue Wang,[a] Xiaoyi Zhang,[a] Jinxuan Pang,[a] Chang Li*[bc] and Shiying Tang*[a]

Mercury ions (Hg^{2+}) are highly toxic and bioaccumulative, posing a serious threat to the environment and human health. Traditional analytical techniques are limited by cost, portability and real-time monitoring capabilities, and there is an urgent need for sensitive and portable detection methods. In this study, copper nanoclusters (CuNCs) were encapsulated in red-emitting europium metal–organic frameworks (Eu-MOFs), and a ratiometric fluorescence probe based on CuNCs@EuMOFs was constructed and used for the detection of Hg^{2+} in water extracts of traditional Chinese medicine samples and river samples. In the presence of Hg^{2+}, the fluorescence of this probe is enhanced at 450 nm and weakened at 618 nm. Visual quantification can be performed using a smart phone based on the color change. The linear range is 0–360 μM (R^2 = 0.9986), and the detection limit is 0.94 nM. The sample recovery rate was 94.43–106.43% (RSD < 4.37%). This study provides a new strategy for the portable visual detection of Hg^{2+} in complex matrices.

Received 9th June 2025
Accepted 11th September 2025

DOI: 10.1039/d5ra04013b

rsc.li/rsc-advances

1. Introduction

Heavy metal mercury (Hg) is highly toxic and widely distributed in the natural environment.[1] In environments affected by human activities, mercury primarily exists in three chemical forms: elemental mercury (Hg^0), organic mercury compounds (CH_3Hg^+ and $C_2H_5Hg^+$), and inorganic mercury compounds (such as Hg^{2+} and Hg^+). Among these, due to its low density, high toxicity, carcinogenicity, and bioaccumulation potential, Hg^{2+} poses a great threat to the environment and human health.[2] The accelerated pace of industrialization has expanded the applications and production of mercury, leading to its increased release into the natural environment through human activities. In nature, Hg^{2+} is resistant to biodegradation, causing it to persist, circulate, and accumulate within various environmental media such as air, water, and soil. This persistence allows Hg^{2+} to remain in the environment long-term and enter biological organisms *via* food chains or inhalation. Even at relatively low concentrations, Hg^{2+} poses serious health risks.[3] Mercury exposure can inflict irreversible damage on essential organs such as the liver, kidneys, and lungs, as well as cause severe disturbances in the nervous and immune systems. Chronic exposure may lead to debilitating diseases, including Minamata disease, acrodynia (also known as pink disease), and Alzheimer's disease.[4] Consequently, the development of innovative methods for the simple, highly sensitive, and selective detection of Hg^{2+} is of critical importance.

Currently, the traditional analytical approaches employed for the detection of Hg^{2+} mainly encompass atomic absorption spectrometry,[5] atomic fluorescence spectrometry,[6] inductively coupled plasma mass spectrometry,[7] and high-performance liquid chromatography-inductively coupled plasma mass spectrometry.[8] These methods exhibit high sensitivity and low detection limits; however, they typically entail complex sample pretreatment and high instrument maintenance costs.[9] Meanwhile, the reproducibility of emerging electrochemical methods[10] requires improvement. Fluorescent sensors boast numerous advantages, such as material diversity, low cost, rapid response, ease of operation, and high sensitivity,[11] and have gradually emerged as a more appealing alternative approach. The luminescent materials of the fluorescence sensor mainly consist of carbon dots,[12] metal–organic skeleton,[13] quantum dots,[14] organic fluorescent dyes,[15] and luminous metal nanoclusters.[16] Among them, metal nanoclusters demonstrate extensive application potential in bioimaging, medical diagnosis, chemical sensing, nanomedicine preparation, and biomolecular recognition due to their attributes like tiny size, low toxicity, high-brightness fluorescence, excellent light stability, and good biocompatibility.[17] At present, gold nanoclusters (AuNCs),[18] silver nanoclusters (AgNCs),[19] platinum

[a]*Hebei Key Laboratory of TCM Research and Development, College of Traditional Chinese Medicine, Chengde Medical University, Chengde 067000, China. E-mail: wangchenfeng@cdmc.edu.cn; tangshiying@cdmc.edu.cn*

[b]*NMPA Key Laboratory for Research and Evaluation of Pharmaceutical Preparation and Excipients, China Pharmaceutical University, Nanjing 210009, China. E-mail: lichang982003@163.com*

[c]*School of Pharmacy, Tianjin Medical University, Tianjin 300070, China*

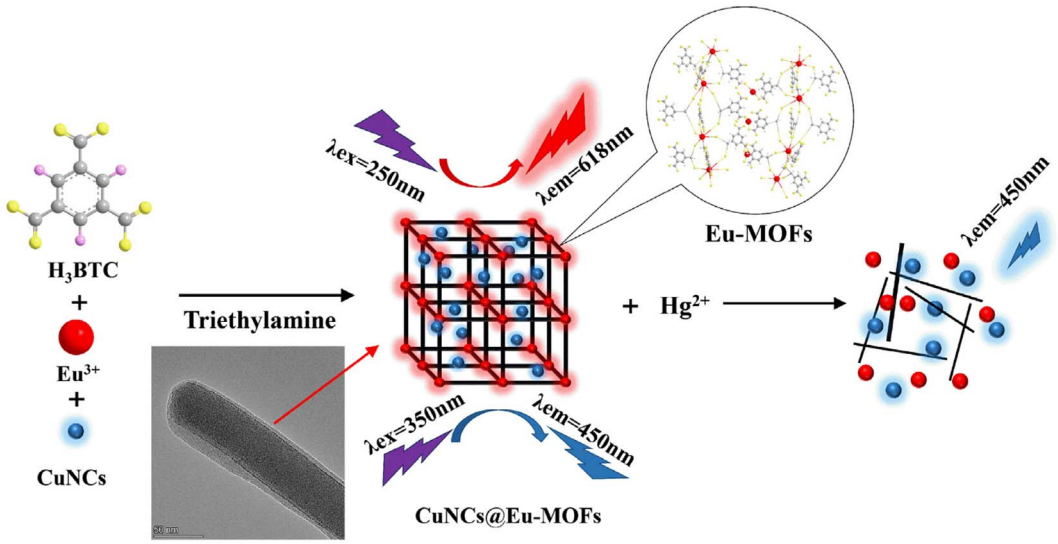

Scheme 1 Synthesis of the dual-emission fluorescent nanoprobe CuNCs@Eu-MOF and its detection mechanism for Hg^{2+}.

nanoclusters (PtNCs),[20] and copper nanoclusters (CuNCs)[21] are widely utilized. Compared to AuNCs, AgNCs, and PtNCs, CuNCs offer not only a high quantum yield and strong biocompatibility but also a cost-effective production process.

To achieve the rapid detection of Hg^{2+} in diverse environments, researchers have devoted considerable efforts to the development of fluorescence detection methods based on metal nanoclusters. Nevertheless, the majority of current fluorescence sensors mainly depend on the alterations in the fluorescence intensity of a single-colour to indicate the presence of Hg^{2+}. This single-colour fluorescence test is highly vulnerable to external environmental factors, which have an impact on the accuracy and reliability of the test. In light of this limitation, it has emerged as an important research direction to develop a ratio fluorescence sensor featuring dual emission characteristics, accompanied by obvious fluorescence colour changes during the detection process. By simultaneously monitoring the changes in fluorescence intensity at two distinct wavelengths and calculating their ratio to reflect the concentration of Hg^{2+}, such sensors can significantly reduce the interference of external environmental factors and enhance the accuracy and stability of the detection.[22] Despite its considerable potential, there are numerous challenges in developing an Hg^{2+} detection sensor of efficient and environmentally friendly. Therefore, the design of a simple and readily available double-emission ratio fluorescent probe for the visual detection of Hg^{2+} is an urgent requirement for current research.

In recent years, notable advancements have been achieved in creating dual-emission fluorescence systems utilizing metal nanoclusters (MNCs) combined with other materials. For instance, Liu's team synthesized single-emission s-AuNCs using chloroauric acid and glutathione, followed by the addition of 11-mercaptoundecanoic acid under alkaline conditions to produce dual-emission AuNCs (d-AuNCs) with emissions at 420 nm and 630 nm. These d-AuNCs were successfully applied for intracellular sensing and imaging of valine and Cr^{3+}.[23] In another study, scientists developed dual-emission fluorescent nanocomposites based on silver nanoclusters prepared *via* electrostatic self-assembly. These nanoprobes exhibited excellent water solubility and stability and were employed for the selective and sensitive detection of copper ions.[24] Building on these advancements, researchers have combined metal nanoclusters with metal–organic frameworks (MOFs) to construct novel fluorescent sensors for the highly sensitive detection of metal ions.[25,26] MOFs formed by the coordination of metal ions and organic ligands offer several benefits, including high loading capacity, extensive specific surface area, customizable pore size, adjustable emission characteristics, and well-defined nanostructures.[27] Among them, lanthanide-based metal–organic frameworks (Ln-MOFs) not only inherit the general advantages of MOFs but also exhibit the unique fluorescence properties of lanthanide ions, demonstrating tremendous potential in the field of inorganic ion sensing.[28]

Inspired by these findings, we introduced CuNCs[29] into the Eu-MOF synthesis environment *via* a one-pot method (Scheme 1). This process produced the fluorescent composite CuNCs@Eu-MOFs, which retains the luminescent properties of both Eu^{3+} ions and CuNCs while exhibiting excellent structural and fluorescence stability in aqueous solutions. These features allow Eu-MOF and CuNCs to serve as recognition and reference units, respectively, forming a ratiometric fluorescence sensor for Hg^{2+} detection. The sensor showed promising applicability for Hg^{2+} detection in real samples, providing a new approach for Hg^{2+} sensing and expanding the potential of metal nanoclusters and MOF composites in chemical sensing applications.

2. Materials and methods

2.1. Materials and reagents

All chemicals were of analytical purity and used without further purification. The following reagents were procured from Shanghai Aladdin Biochemical Technology Co., Ltd:

europium(III) chloride hexahydrate ($EuCl_3 \cdot 6H_2O$), L-cysteine, copper(II) sulfate pentahydrate ($CuSO_4 \cdot 5H_2O$), sodium hydroxide (NaOH), trimesic acid (BTC), mercury(II) sulfate ($HgSO_4$), mercurous chloride (Hg_2Cl_2), magnesium chloride hexahydrate ($MgCl_2 \cdot 6H_2O$), aluminum nitrate nonahydrate ($Al(NO_3)_3 \cdot 9H_2O$), disodium hydrogen phosphate dodecahydrate ($Na_2HPO_4 \cdot 12H_2O$), and sodium dihydrogen phosphate dihydrate ($NaH_2PO_4 \cdot 2H_2O$). Sodium chloride (NaCl) was purchased from Beijing Solarbio Science & Technology Co., Ltd, whereas barium chloride ($BaCl_2$) and lead(II) acetate trihydrate ($Pb(CH_3COO)_2 \cdot 3H_2O$) were obtained from Tianjin Standard Technology Co., Ltd. Potassium hydroxide (KOH) and iron(III) chloride ($FeCl_3$) were provided by Tianjin Kemio Chemical Reagent Co., Ltd. Methanol and ethanol were supplied by Fuchen (Tianjin) Chemical Reagent Co., Ltd. Acetonitrile was purchased from Thermo Fisher Scientific (China) Co., Ltd. Isopropanol was purchased from Tianjin Kemiou Chemical Reagent Co., Ltd, China. Ultrapure water was employed for preparing all aqueous solutions, and dialysis membranes with a molecular weight cutoff of 1000 Da were sourced from Hunan YiBo Biotechnology Co., Ltd.

2.2. Instruments

Fluorescence spectroscopy was conducted using a Hitachi F-7100 spectrophotometer (Hitachi, Japan) equipped with a standard 1 cm quartz cell. Fourier transform infrared spectrometer (FT-IR) analysis was carried out on a Shimadzu IRAffinity-1S WL spectrometer (Shimadzu, Japan) to characterize functional groups. Morphological characterization was performed using high-resolution electron microscopy: scanning electron microscopy (SEM) images were acquired on a Thermo Fisher Apreo S instrument (Thermo Fisher, USA), while transmission electron microscopy (TEM) was conducted on an FEI Talos F200X microscope (FEI, USA). X-ray photoelectron spectroscopy (XPS) data were acquired using a Super X X-ray photoelectron spectrometer (Thermo Fisher, USA), and X-ray diffraction (XRD) patterns were recorded with a SmartLab3 X-ray diffractometer (Rigaku, Japan). Particle size measurement and zeta potential analysis of the materials were performed using a Malvern Panalytical Zen3690 Laser Diffraction Particle Size Analyzer (Malvern Panalytical, UK). Additional equipment used included an MHS4pro heating magnetic stirrer (JoanLab, Zhejiang Quanan Scientific Instruments, China), an AG-245 electronic balance (METTLER TOLEDO), a PHS-3C pH meter (Shanghai INESA Scientific Instrument Co., Ltd, China), a KQ-700 ultrasonic cleaner (Kunshan Ultrasonic Instruments Co., Ltd, China), a H/T18MM benchtop high-speed centrifuge (Hunan Hexi Instrument Equipment Co., Ltd, China), Concentrator Vacuum Centrifugal CV200 (BEIJING JM TECHNOLOGY CO., Ltd, China), and an SC-15 digital super thermostatic bath (Ningbo Xinzhi Biotechnology Co., Ltd, China).

2.3. CuNCs@Eu-MOFs preparation of nanoprobes

2.3.1. Preparation of CuNCs. CuNCs were synthesized according to a previously reported method.[29] Specifically, 2.5 mL of 1 mM $CuSO_4$ solution was added to 25 mL of 35 mg mL^{-1} L-cysteine (L-Cys) solution and stirred at room temperature for 10 minutes. Following this, 1 mL of 0.4 M NaOH solution was introduced into the mixture, which was then stirred at 55 °C for 4.5 hours. A color change to pale yellow indicated the successful synthesis of CuNCs. The resulting solution was filtered using a 0.22 μm aqueous filter membrane to remove residual impurities. Subsequently, the solution was dialyzed in deionized water for 24 hours using a 1000 MWCO dialysis membrane to eliminate unreacted small molecules. The final CuNCs solution was stored at 4 °C for preservation.

2.3.2. Preparation of CuNCs@Eu-MOFs. CuNCs@Eu-MOFs were synthesized with slight modifications based on a previously established method.[30] A methanol solution (10 mL) containing 21 mg of BTC, 1 mL of CuNCs dispersion, and 36.7 mg of $EuCl_3 \cdot 6H_2O$ was vigorously stirred for 30 min. After adding 200 μL of triethylamine, the mixture was allowed to react undisturbed at room temperature for 2 h. The resulting CuNCs@Eu-MOFs composite was isolated by centrifugation (8000 rpm, 10 min), purified *via* three ethanol washes, and dried under vacuum at 45 °C to obtain a brown powder.

For comparison, Eu-MOFs were prepared using the same procedure as CuNCs@Eu-MOFs, except without the addition of CuNCs, resulting in a white Eu-MOFs powder.

2.4. Detection of Hg^{2+}

The CuNCs@Eu-MOFs sample (4 mg) was accurately weighed and dispersed in 4 mL deionized water. The mixture was sonicated for 10 minutes to ensure uniformity, achieving a final concentration of 1 mg mL^{-1}. Subsequently, 400 μL of this CuNCs@Eu-MOFs suspension was placed into a clean quartz cuvette, followed by the addition of 500 μL of a known concentration Hg^{2+} aqueous solution. 100 μL deionized water was added to make the final volume of 1 mL. The reaction was carried out at room temperature for 10 minutes. The fluorescence emission spectra were recorded under the excitation wavelengths of $\lambda_{ex} = 350$ nm and $\lambda_{ex} = 250$ nm, and the excitation and emission slit widths were both 10 nm.

2.5. Detection of Hg^{2+} in actual samples

To assess the practical application potential of the sensor, the performance of the CuNCs@Eu-MOFs ratiometric fluorescence probe was tested in real samples using the standard recovery method. In this experiment, tap water and water extract of *Atractylodes* were used as the real sample model, and the samples were pretreated as follows before the experimental study of standard recovery:

2.5.1. River water samples. Determination of Hg^{2+} content in river water using a ratio fluorescent probe CuNCs@Eu-MOFs. River water samples were collected from Wulie River, Chengde City, Hebei Province, China. The water samples were filtered with a 0.22 μm microporous filter membrane to remove suspended particles, and then Hg^{2+} solutions of different concentrations were added. CuNCs@Eu-MOFs and Hg^{2+} added with different concentrations were incubated in the river water sample together for 10 min, then recorded the fluorescence spectra. The fluorescence spectra were tested three times, and

the average values were obtained. The fluorescence spectra were measured to obtain F_{450}/F_{618} values, and the Hg^{2+} content in real sample river water was determined according to the obtained working curve. Test three times and take the average.

2.5.2. Water extracts of traditional Chinese medicine samples. Detection of Hg^{2+} in *Atractylodes* (collected from Shangluo City, Shanxi Province, China) using the ratiometric fluorescence probe CuNCs@Eu-MOFs. The dried *Atractylodes* rhizomes were placed in a grinder for thorough pulverization, and the resulting powder was sieved through a 100-mesh screen and collected. Accurately weighed 50 mg of the *Atractylodes* powder was added to 5 mL of deionized water, subjected to ultrasonication for 10 minutes, then centrifuged at 10 000 rpm for another 10 minutes. The resulting supernatant was then filtered through a water-soluble membrane filter (0.22 μm), sealed, and stored at 4 °C. The final solution was diluted with water at a ratio of 1 : 100 (v/v) to serve as the TCM sample. Subsequently, the CuNCs@Eu-MOFs probe and various concentrations of Hg^{2+} were incubated with the TCM sample for 10 minutes. Recorded the fluorescence spectra under the same conditions as those used for detecting Hg^{2+} in standard solutions, and this process was repeated three times.

2.6. Detect Hg^{2+} on a smartphone platform

After adding Hg^{2+} to the CuNCs@Eu-MOFs system, the fluorescence intensity at 450 nm increases, while the emission intensity at 618 nm decreases, resulting in a distinct color change. This ratiometric response is quantified by analyzing the B/R (blue-to-red) intensity ratio. For visual verification, the probe solution is photographed under 254 nm UV light using a smartphone. All photographing processes are conducted under completely dark conditions (in a dark box) to ensure no interference from ambient light. In terms of standardizing camera settings, fixed parameters are adopted (focal length 5.59 mm, f/1.88 aperture, ISO 5917, 1/5 s exposure, automatic white balance), and all sample collection processes remain consistent. For background correction, blank control (no sample) images are synchronously collected during photographing as background templates, and background subtraction is performed using ImageJ's ROI analysis. Finally, RGB values are extracted through the Color Picker app for colorimetric analysis. To ensure the reliability of the measurement, the average B/R ratio is calculated from three randomly selected regions in each image.

3. Results and discussion

3.1. Characterization of CuNCs@Eu-MOFs

To investigate the morphological characteristics and particle size of CuNCs@Eu-MOFs, The morphology of the material was characterized by SEM and TEM. SEM images revealed that the CuNCs predominantly formed irregularly shaped nanoparticles, which were efficiently encapsulated with L-Cys (Fig. 1A). TEM analysis further validated that the CuNCs were uniformly dispersed and exhibited a well-defined distribution in the solution (Fig. 1C).

Compared with SEM images of Eu-MOFs, we can see that CuNCs@Eu-MOFs have obvious morphological changes. Eu-MOFs exhibit a typical rod-like crystal structure (Fig. S1), while CuNCs@Eu-MOFs exhibit a grass-like crystal structure ranging in width from 0.01 to 0.18 mm (Fig. 1B and E). This morphological change may be since in the process of aqueous phase synthesis, water not only participates in the formation of CuNCs@Eu-MOFs crystal as a reactant but also affects the growth kinetics and physicochemical properties of the crystal, thus determining the final crystal shape.[31] As observed in the SEM images (Fig. S2), both Eu-MOF and CuNCs@Eu-MOF display a smooth surface morphology, without any noticeable roughening that would be indicative of CuNCs adsorption on the surface. This morphological feature suggests that CuNCs are not loaded onto the Eu-MOF surface through an adsorption

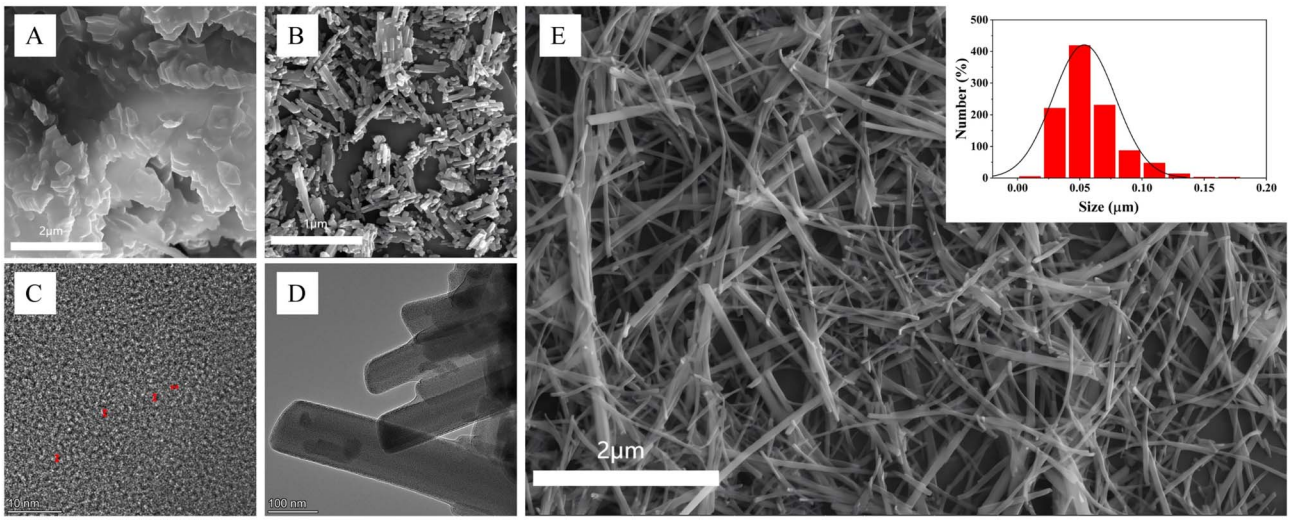

Fig. 1 Morphological characterization of (A and C) CuNCs and (B and D) Eu-MOFs by SEM and TEM imaging. (E) SEM micrograph of the CuNCs@Eu-MOFs composite, with corresponding width size distribution shown in the inset.

mechanism. Instead, they are more likely to be encapsulated within the internal framework of Eu-MOF, thereby exerting no significant influence on its surface topography.

As can be seen from the fluorescence intensity-size distribution diagram (Fig. S3), the single-component CuNCs and Eu-MOF exhibit characteristic fluorescence peaks in the size ranges of 847 ± 33.3 nm and 2031 ± 239 nm, respectively, reflecting their respective fluorescence-size response characteristics. The composite system CuNCs@Eu-MOF formed by coating CuNCs on Eu-MOF, due to structural coupling, reshapes the fluorescence-size correlation, and shows a unique fluorescence behavior in the size range of 5296.3 ± 899.9 nm, which is significantly different from that of the single-components, indirectly verifying the construction of the coated structure. After the introduction of Hg^{2+}, the fluorescence-size response range of the CuNCs@Eu-MOF + Hg^{2+} system changes to 2849 ± 11.2 nm, which is different from that without the introduction. This reflects that the interaction between Hg^{2+} and the composite system changes the fluorescence-size dependence relationship, providing a research basis for applications such as Hg^{2+} sensing based on the fluorescence size effect (for example, using the size-related fluorescence change to detect Hg^{2+}), and also reflects the response characteristics of the composite system to specific ions. In conclusion, the composite system constructed by coating CuNCs on Eu-MOF, due to the change of the microstructure (supported by SEM, although the details of the composite structure are not directly presented in the figure, the performance differences are indirectly related), leads to the alienation of the fluorescence – size response, and can be further regulated by the interaction with Hg^{2+}. This not only proves the construction of the coated structure but also shows its potential in applications such as ion sensing.

In addition, the energy dispersive spectroscopy (EDS) was used to analyze the element composition of CuNCs@Eu-MOFs (Fig. S4). The detected N, S, and Cu elements in the EDS spectrum confirm that CuNCs are successfully encapsulated in the structure of CuNCs@Eu-MOFs. This result provides a reliable basis for the morphology and composition for the subsequent detection of Hg^{2+} using this composite material. The zeta potential diagram (Fig. S5) directly reflects the surface charge state of the material. The characteristic peak of CuNCs (−35.6 mV) reflects its inherent surface charge. After constructing CuNCs@Eu-MOF, the zeta potential shifts, which proves that Eu-MOF and CuNCs are successfully combined, and the surface chemical environment is changed.

To further elucidate the crystallographic characteristics of CuNCs@Eu-MOFs, Eu-MOFs, and CuNCs, an XRD analysis was conducted. The XRD spectrum of CuNCs displayed several sharp diffraction peaks, indicative of a high level of crystallinity. In contrast, the diffraction peaks of Eu-MOFs were less intense and the pattern was generally smoother, suggesting a lower crystallinity in Eu-MOFs. This contrast in crystallinity between Eu-MOFs and CuNCs likely reflects the intrinsic structural complexity of MOFs or a more disordered crystal structure in Eu-MOFs. The XRD spectrum of CuNCs@Eu-MOFs showed similarity to that of Eu-MOFs, with an absence of distinct CuNCs peaks, implying that the CuNCs may be well encapsulated within the Eu-MOFs. This encapsulation could prevent the detection of CuNCs diffraction signals, or the dispersion of CuNCs within the Eu-MOFs pores might lead to a decrease in overall crystallinity. The comparison of XRD spectra among the three materials suggests that the encapsulation of CuNCs greatly changed the structure of Eu-MOFs. The analysis indicates that the XRD features of the CuNCs@Eu-MOFs composite are predominantly those of Eu-MOFs, with the characteristic peaks of CuNCs being obscured, indicating effective encapsulation of CuNCs by Eu-MOFs.

The FT-IR spectra of CuNCs@Eu-MOFs, Eu-MOFs, BTC, CuNCs, and L-Cys are presented in Fig. 2B. In the spectra of L-Cys and CuNCs, the broad absorption band observed between 3300–3400 cm^{-1} is ascribed to the N–H stretching vibrations of hydroxyl (–OH) or amine (–NH) groups. The absorption peak at 2551.82 cm^{-1} in L-Cys corresponds to the stretching vibration of –SH, which is absent in the CuNCs spectrum, indicating the copper atom forms a Cu–S bond with the –SH group.[29] The characteristic absorption bands of BTC reveal distinct vibrational modes, a strong C=O stretch at 1600 cm^{-1}, aromatic C=C framework vibrations between 1500–1600 cm^{-1}, and C–O stretching modes in the 1200–1300 cm^{-1} region. The peak around 1000 cm^{-1} is due to the bending vibration of C–H. In the

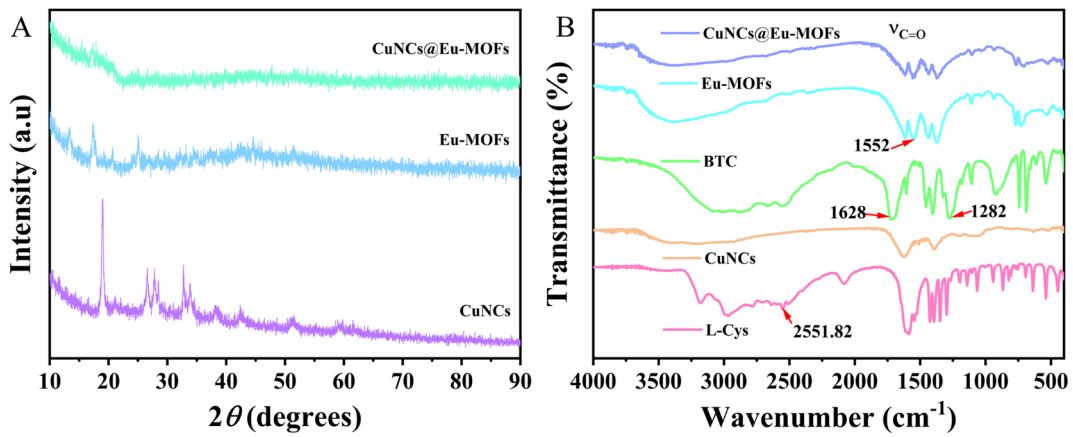

Fig. 2 (A) XRD patterns of CuNCs@Eu-MOFs, Eu-MOFs and CuNCs. (B) FT-IR spectra of CuNCs@Eu-MOFs, Eu-MOFs, BTC, CuNCs and L-Cys.

spectrum of Eu-MOF, the C=O peak is shifted and weakened because of the coordination of Eu^{3+} with the carboxylate groups.[32] A vibration peak of Eu–O appears in the region of 500–600 cm^{-1}, which is not present in the BTC spectrum, suggesting the coordination of Eu^{3+} with the oxygen atoms of the carboxylate groups. In the spectrum of CuNCs@Eu-MOFs, the C=O stretching vibration peak at 1600 cm^{-1} is similar to that of Eu-MOF but may exhibit a slight shift. In the 500–600 cm^{-1} region, the vibration of Eu–O bonds is observed, along with the characteristics of Cu–S bonds. FT-IR analysis reveals that CuNCs@Eu-MOFs retain the main structural features of Eu-MOF, and due to the addition of copper nanoclusters, the material exhibits vibration characteristics of Cu–S or Cu–O in the low wavenumber region, which further enhances the composite's properties.

To reveal the elemental compositions of CuNCs@Eu-MOFs, Eu-MOFs, and CuNCs, these solid powder samples were analyzed by XPS. The relevant results are shown in Fig. 3. In the full-scan XPS spectrum of Fig. 3A, CuNCs@Eu-MOFs, and Eu-MOFs both show three major peaks, corresponding to Eu 3d (1135.06 eV), O 1s (531.47 eV), and C 1s (284.86 eV), respectively. It is confirmed that the element CuNCs@Eu-MOFs is consistent with its raw material. To analyze the chemical state of each element in detail, the XPS spectra were fitted by peaks. Fig. 3B shows the high-resolution XPS spectrum of C 1s, which is fitted to obtain three peaks corresponding to 284.99 eV (C–C/C–H), 286.07 eV (C–O–C), and 288.78 eV (O–C=O), indicating that the C element in Eu-MOF exists in these three chemical states. Fig. 3C shows the O 1s high-resolution XPS spectrum fitting two peaks at 531.66 eV (C–O/Eu–O) and 533.24 eV (C=O).[33] Notably, an additional peak of 534.32 eV was observed in the O 1s spectrum of CuNCs, possibly attributed to the O–FX bond. During the wrapping process, the peak intensity of the S element is reduced (Fig. 3E–G), which may indicate that the S element is involved in a chemical reaction during the wrapping process. As for the Cu element, its characteristic peak is not detected when CuNCs are encased in Eu-MOFs, which may be related to signal shielding, interference or changes in CuNCs during the encased process. However, a characteristic peak of N 1s similar to CuNCs is found in the XPS spectrum of CuNCs@Eu-MOFs. Through XPS analysis, we not only confirm the composition of elements in CuNCs@Eu-MOFs, Eu-MOFs and CuNCs, but also gain insight into the chemical states of these elements in the samples.

CuNCs exhibit intense blue fluorescence due to their unique physicochemical properties, with an emission peak at 460 nm, as shown in Fig. S6. When CuNCs are encapsulated within Eu-MOF to form the CuNCs@Eu-MOFs composite, the fluorescence intensity is reduced. In the fluorescence spectrum shown in Fig. S6, with an excitation wavelength of 350 nm, CuNCs@Eu-MOFs display a weaker emission peak at 450 nm, indicating that the original strong emission peak at 460 nm has shifted to 450 nm, with a decrease in fluorescence intensity, which may be a result of the interaction between CuNCs and Eu-MOF. The emission profile of the CuNCs@Eu-MOFs probe exhibits multiple distinct peaks, the dominant CuNCs emission at 450 nm, and three characteristic Eu^{3+} transitions at 590, 619, and 696 nm (Fig. S6 and S7). This composite spectrum confirms the successful integration of both luminescent components. It is noteworthy that the high-intensity fluorescence at 450 nm

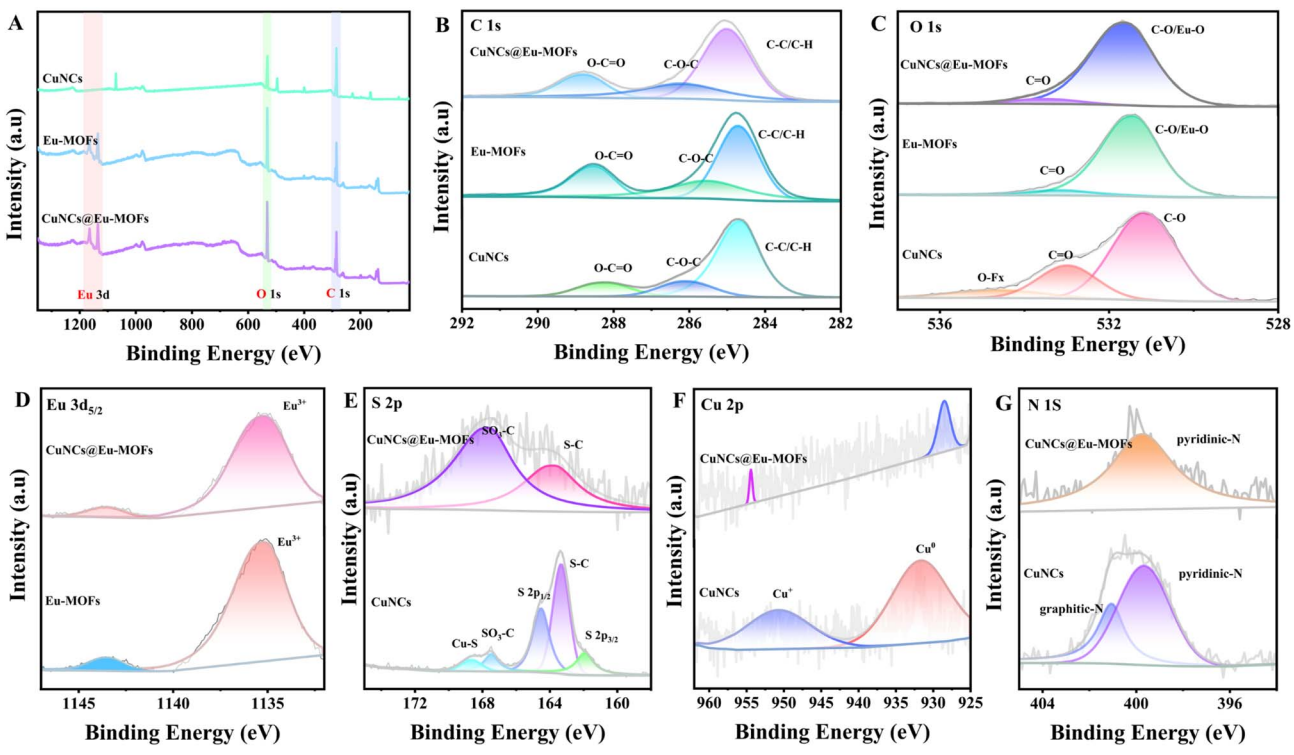

Fig. 3 (A) Full-scan XPS spectra of CuNCs, Eu-MOFs and CuNCs@Eu-MOFs, (B) C 1s, (C) O 1s, (D) Eu $3d_{5/2}$, (E) S 2p, (F) Cu 2p, (G) N 1s.

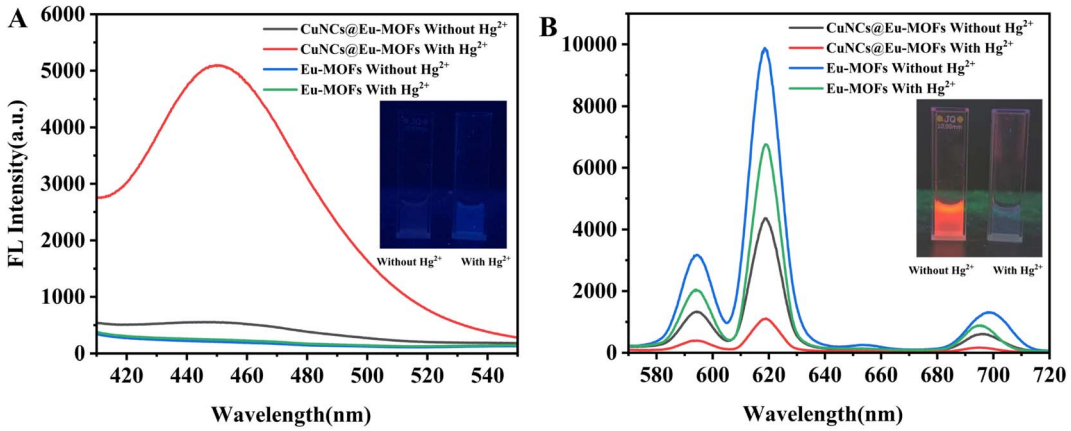

Fig. 4 Fluorescence spectra of CuNCs@Eu-MOFs and Eu-MOFs in the presence and absence of Hg^{2+} (A) λ_{ex} = 350 nm, (B) λ_{ex} = 250 nm.

and 618 nm does not originate from a simple mixture of $CuSO_4$, L-Cys, $EuCl_3$, or H_3BTC, but rather from the inherent properties of CuNCs and Eu-MOF. To visually demonstrate the fluorescence properties of CuNCs@Eu-MOFs, the study also observed the color changes of the suspension under different UV light. Under 365 nm UV light, the suspension appears blue, while under 254 nm UV light, it exhibits a bright red color. These findings, as depicted in the insets of Fig. 4A and B, provide additional evidence that CuNCs are effectively encapsulated within the cavities of the Eu-MOF structure.

3.2. Fluorescence properties of CuNCs@Eu-MOFs

Before assembly into the composite material, CuNCs exhibited pronounced blue fluorescence with an emission peak at 460 nm (Fig S6), while Eu-MOF displayed its characteristic red fluorescence due to the antenna effect, with an emission peak at 618 nm (Fig. S7D). As shown in Fig. S6A and B, the characteristic peak of CuNCs disappeared after encapsulation within Eu-MOF, which could be attributed to quenching due to aggregation, ligand effects, or energy transfer. The addition of mercury ions led to an enhancement of the characteristic peak, possibly due to the interaction between mercury ions and CuNCs, competitive action with Eu-MOF, or the introduction of a new energy transfer pathway. These interactions altered the local environment of Eu-MOF and the luminescence state of CuNCs, enabling the detection of mercury ions.

Fig. 4A and B show that the prepared CuNCs@Eu-MOFs exhibited emission characteristics of both CuNCs and Eu^{3+}. Notably, the intensity of the dual emission was closely related to the volume of CuNCs added, with the intensity ratio (F_{450}/F_{618}) of CuNCs to Eu-MOFs reaching its maximum when 1 mL of CuNCs was added (Fig. S8). As the concentration of CuNCs increased during synthesis, the emission band of Eu-MOF is slightly weakened, which may be due to the coordination of carboxylic acid groups in CuNCs with Eu^{3+} centers. According to the antenna effect, the energy transfer efficiency of the initial ligand BTC to Eu^{3+} decreases, thereby decreasing the characteristic emission intensity of Eu^{3+}.[34]

Under 350 nm excitation, CuNCs@Eu-MOFs exhibited maximum fluorescence intensity, with the blue emission (Fig. S7) confirming its origin from the CuNCs component. At 250 nm excitation, CuNCs@Eu-MOFs displayed three characteristic peaks corresponding to the transitions of Eu^{3+} at $5D_0 \rightarrow 7F_1$, $5D_0 \rightarrow 7F_2$, and $5D_0 \rightarrow 7F_4$ (Fig. S7E).[3] The excitation spectrum of CuNCs@Eu-MOFs at 620 nm emission primarily showed a peak at 250 nm (Fig. S7B). Eu-MOFs displayed excitation wavelength-dependent emission intensity, reaching maximum fluorescence at 250 nm (Fig. S7F).

Prior to Hg^{2+} sensing applications, rigorous stability assessments were conducted to verify the probe's performance in aqueous media. The CuNCs@Eu-MOFs composite demonstrated maintained luminescence and structural stability under varying physicochemical conditions, such as solvent composition, analyte concentration, pH 2–12, 20–80 °C, and 30 day storage (Fig. S9–S14). The fluorescence intensity ratio (F_{450}/F_{618}) was higher under neutral conditions, indicating that CuNCs@Eu-MOFs are suitable for use in a neutral environment. Fig. S15 shows the fluorescence intensity ratio (F_{450}/F_{618}) of three different batches of CuNCs@Eu-MOFs, demonstrating the good reproducibility of the synthesis process.

3.3. Fluorescence detection of Hg^{2+}

In the detection system, varying concentrations of Hg^{2+} ions led to changes in fluorescence intensity, as depicted in Fig. 5A–E. As the Hg^{2+} concentration increased from 0 to 360 μM, the fluorescence intensity at F_{618} gradually decreased, while the fluorescence intensity at F_{618} gradually increased, indicating that the CuNCs@Eu-MOFs material had a significant response to Hg^{2+} and the fluorescence intensity ratio (F_{450}/F_{618}) showed a strong linear correlation with Hg^{2+} concentration (Fig. 5). In the concentration range of 0 to 360 μM, the response values displayed a linear positive relationship, with the regression equation being $Y = 0.00113X + 0.08735$ ($R = 0.9986$), where X represents the Hg^{2+} concentration in μM. Additionally, the probe demonstrated exceptional sensitivity, achieving a detection limit (LOD) of 0.94 nM and quantification limit (LOQ) of 3.12 nM. A comparison with previously reported fluorescent

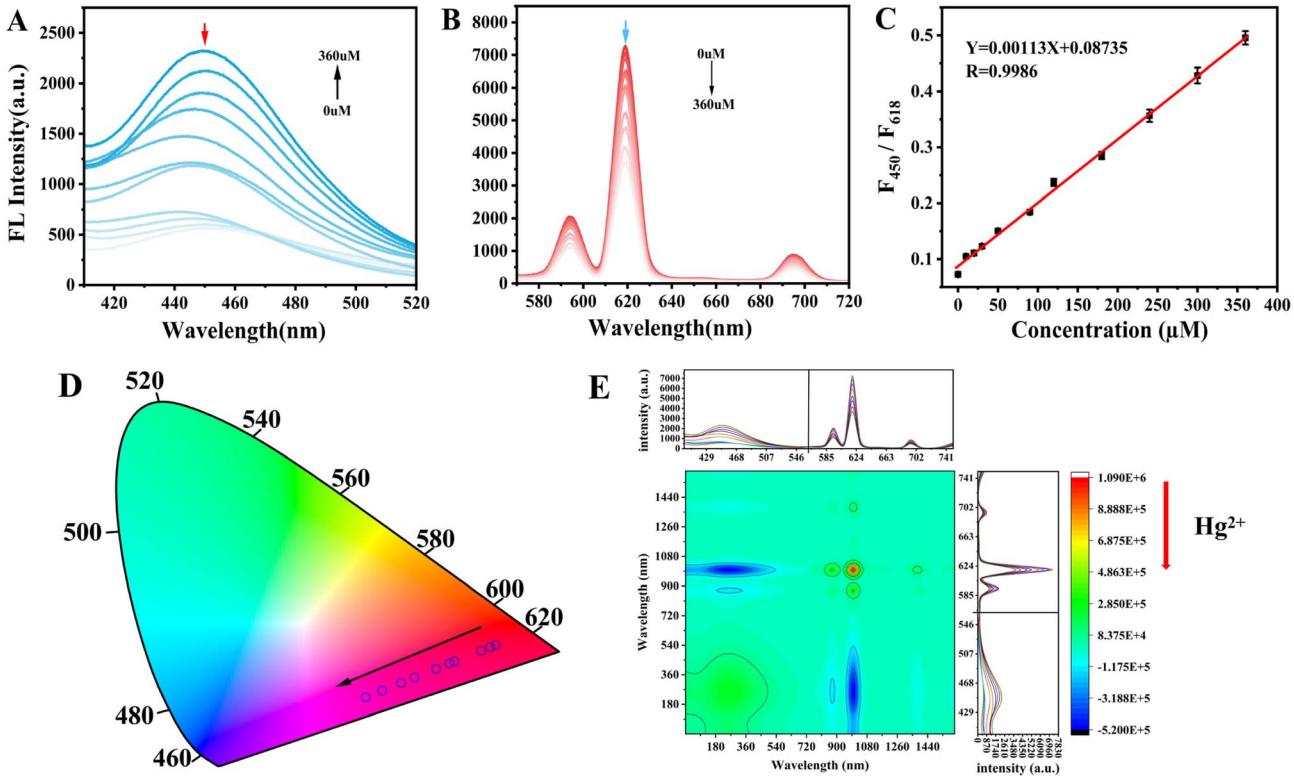

Fig. 5 (A) $\lambda_{ex} = 350$ nm, (B) $\lambda_{ex} = 250$ nm CuNCs@Eu-MOFs fluorescence spectra with different Hg^{2+}; (C) F_{450}/F_{618} ratio *vs.* Hg^{2+} linear curve; (D) CIE chromaticity coordinates (colorimetric response); (E) probe fluorescence intensity *vs.* Hg^{2+} correlation.

sensors for Hg^{2+} detection (Table S1) showed that this method outperforms several others in terms of sensitivity, detection range, and potential applications, further supporting the CuNCs@Eu-MOFs-based ratiometric fluorescent sensor as a promising tool for Hg^{2+} detection in aqueous environments.

In order to determine the binding stoichiometry and binding strength of Hg^{2+} to CuNCs@Eu-MOF, the fluorescence response data were fitted with Stern–Volmer (S–V) equation and Benesi–Hildebrand (B–H) equation models, respectively. As shown in Fig. S16, S–V analysis indicated that the 1 : 1 binding model exhibited excellent fitting performance with a high determination coefficient (R^2) of 0.9983. The fitted equation was $R/R_0 = 0.01539[Q] + 1.2509$, where [Q] represents the concentration of Hg^{2+}. The binding constant K_{S-V}, derived from the slope, was calculated to be 1.539×10^4 M^{-1}, suggesting a moderate binding affinity between Hg^{2+} and the probe. The results of B–H model are shown in Table S2. The 2 : 1 model had the best fitting effect, with R^2 of 0.941, which was significantly better than 0.8831 of the 1 : 1 model and 0.6555 of the 1 : 2 model. The corresponding equation was $y = 16.542x + 0.9791$, where $x = \frac{1}{\sqrt{[Q]}}$ and $y = \sqrt{R - R_0}$. R represents the fluorescence intensity ratio (F_{450}/F_{618}) of CuNCs@Eu-MOF in the presence of different concentrations of Hg^{2+}, and R_0 represents the fluorescence intensity ratio (F_{450}/F_{618}) of CuNCs@Eu-MOF. Although this model suggested the possible presence of a secondary binding site in CuNCs@Eu-MOF, its reliability was considerably lower than that of the 1 : 1 model obtained from the S–V analysis. Overall, the S–V model provided a more reliable quantitative description of the interaction between Hg^{2+} and CuNCs@Eu-MOF. The calculated K_{S-V} value effectively accounts for the high sensitivity and specificity observed in the fluorescence-based detection of Hg^{2+}, even at low concentrations.

As the concentration of Hg^{2+} increased, CuNCs@Eu-MOFs exhibited a noticeable color change under a 254 nm UV lamp. The CIE chromaticity coordinates were derived from fluorescence spectra at varying Hg^{2+} concentrations. As illustrated in Fig. 5D, the CIE coordinates shifted from red (0.6253, 0.2782) to pink (0.4153, 0.1615) as the Hg^{2+} concentration increased from 0 μM to 360 μM, enabling the visual detection of Hg^{2+}.

3.4. Specificity analysis

To evaluate the selectivity of the detection system, the response of common ions to the method developed in this study was examined. Ions such as Mg^{2+}, Cu^{2+}, Al^{3+}, Hg^{+}, Na^{+}, Fe^{3+}, Ba^{2+}, K^{+}, and Pb^{2+} were added at a concentration ten times that of Hg^{2+}, and the fluorescence intensity ratio (F_{450}/F_{618}) was used to represent the degree of influence of various ions on the fluorescence of CuNCs@Eu-MOFs. A higher value indicates a greater influence. The results revealed that except for Cu^{2+}, Al^{3+}, and Fe^{3+}, other metal ions had negligible effects on the fluorescence intensity ratio (F_{450}/F_{618}) (Fig. S17). This indicates that the probe system has excellent anti-interference ability against the most

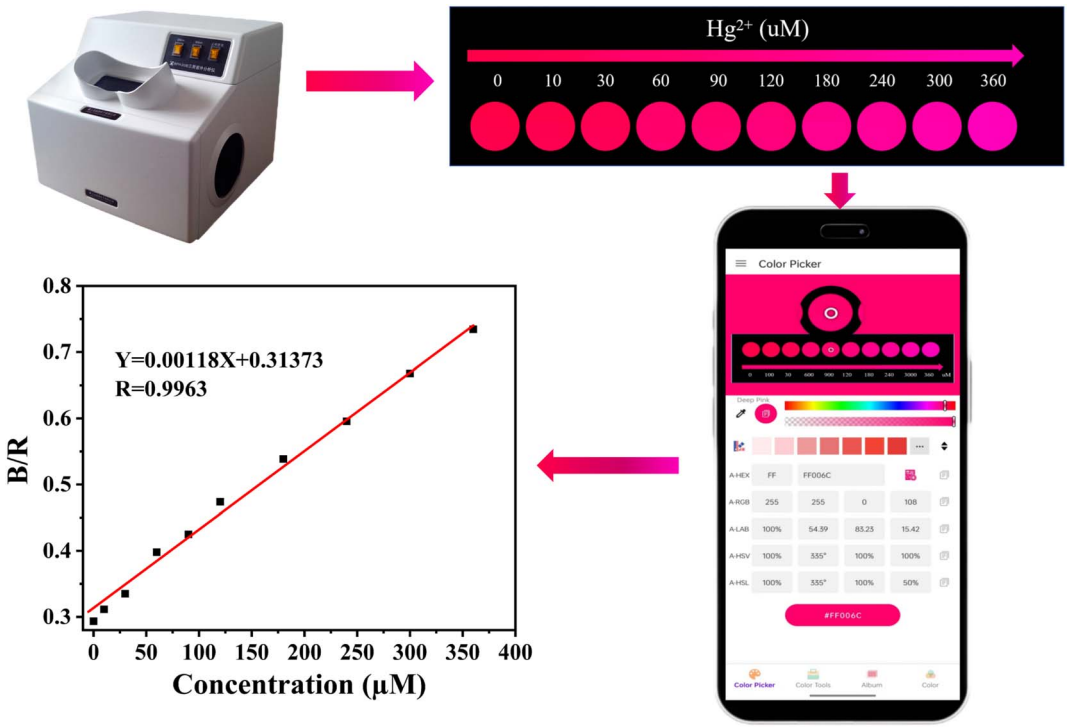

Fig. 6 CuNCs@Eu-MOFs fluorescent color images at different Hg^{2+} concentrations under 254 nm UV light. The ratio graph of red (R) and blue (B) was generated using the color picker app on a smartphone.

common metal ions. Notably, the addition of Cu^{2+}, Al^{3+}, and Fe^{3+} led to a decrease in the characteristic fluorescence peak of CuNCs, reducing the F_{450}/F_{618} ratio, which might be due to the fluorescence quenching caused by the coordination of these metal ions. CuNCs@Eu-MOFs, as an advanced fluorescent probe, not only demonstrates a strong anti-interference ability, effectively resisting interference from most metal ions but also shows its capability for precise detection of specific Hg^{2+} ions in complex environments through its specific fluorescence enhancement response to Hg^{2+}.

3.5. Visual sensing platform for Hg^{2+} detection

Different concentrations of Hg^{2+} solution were added to the prepared probe solution, and after allowing the reaction to complete at room temperature, the solutions were transferred to cuvettes. The smartphone camera captured the corresponding images, and an application was used to automatically detect the RGB values. As shown in Fig. 6, the fluorescence appears red under 254 nm UV light. As the concentration of Hg^{2+} increases, the fluorescence gradually transitions from red to pink. Using the smartphone's Color Picker app under 254 nm UV light, the fluorescence probe solution was exposed to various concentrations of Hg^{2+}, and its color was recorded. The fluorescence colors were then converted into RGB values. The results show that within the 0–360 μM range, a strong linear correlation (R = 0.9963) exists between the Hg^{2+} concentration and the corresponding blue-to-red ratio (B/R). The detection limit was determined to be 2.77 μM, indicating that this method is suitable for visual and quantitative detection of Hg^{2+}.

3.6. Detection of Hg^{2+} in actual samples

To validate the effectiveness of the CuNCs@Eu-MOFs ratiometric fluorescent sensor in real-world applications, the study selected river water and the aqueous extract of the traditional Chinese medicinal herb *Atractylodes* as representative real samples. The aim was to simulate the detection capability of Hg^{2+} ions in complex matrix environments. Using the spike recovery method, the known concentrations of Hg^{2+} standard solutions were added to the river water and *Atractylodes* extract, followed by detection with the CuNCs@Eu-MOFs probe according to the procedures outlined in 2.5. Table 1 presents the detection data results for Hg^{2+} in river water and the *Atractylodes* extract. The recovery rates for Hg^{2+} ranged from 94.43% to 106.43%, with low relative standard deviations (RSD: 0.37–4.37%). The experimental results indicate that the CuNCs@Eu-MOFs ratiometric fluorescent probe not only exhibits excellent sensitivity and accuracy in detecting Hg^{2+} in complex matrices such as river water and the *Atractylodes*extract but also demonstrates good anti-interference ability and potential for practical application. While the sensor's response is primarily to Hg^{2+}, the use of a simple digestion step allows for the determination of total mercury in environmental matrices where organic species might be present. This provides a solid experimental foundation for the application of the CuNCs@Eu-MOFs probe in fields such as environmental monitoring and food safety detection.

3.7. Sensing mechanism analysis

Encapsulation of CuNCs within Eu-MOF to form CuNCs@Eu-MOF composites resulted in a significant quenching of the

Table 1 Recovery rates of Hg^{2+} labeled samples CuNCs@Eu-MOFs

Sample	Added/μM	Detected/μM	Recovery/%	RSD/%
River water	0	—	—	—
	100	97.85	97.85	2.10
	200	206.53	103.26	0.99
	300	285.72	95.24	0.37
Atractylodes	0	—	—	—
water extract	100	99.72	99.72	4.37
	200	188.86	94.43	1.26
	300	319.29	106.43	1.84

characteristic fluorescence of CuNCs in the emission spectra, with the underlying mechanism potentially involving multiple facets. Firstly, the pristine CuNCs exhibited a relatively high negative charge (Fig. S5), indicative of their excellent dispersibility. Upon composite formation, a substantial shift in the zeta potential was observed, suggesting that interfacial interactions between the two components drove the transition of CuNCs toward an aggregated state. This reduction in intermolecular distance subsequently induced aggregation-caused quenching (ACQ). Secondly, during the encapsulation process, BTC ligands might have interacted with CuNCs, thereby altering the surface chemical environment and electronic structure of the latter. Such modifications could have inhibited the transition of excited-state electrons, leading to a diminished fluorescence quantum efficiency. Furthermore, the pronounced discrepancy in zeta potential between CuNCs and CuNCs@Eu-MOF reflected differences in their energy level configurations, which might have established favorable conditions for fluorescence resonance energy transfer (FRET). This process would have enabled the photonic energy absorbed by CuNCs to be transferred to the Eu-MOF matrix rather than being emitted as fluorescence.

When Hg^{2+} was added into the detection system, the intensity of the characteristic fluorescence peak of CuNCs in the emission spectrum was significantly enhanced. Hg^{2+} likely engaged in competitive binding with europium ions within the Eu-MOF framework, partially disrupting the original encapsulation structure. This disruption caused CuNCs to be released from the composite, thereby reducing fluorescence quenching induced by aggregation or energy transfer processes. Concomitantly, the zeta potential of the composite underwent substantial changes, which reshaped the local chemical environment of CuNCs, adjusted their surface charge states and energy level structures, and ultimately promoted electron transition and radiative recombination processes and restoring the characteristic fluorescence emission of CuNCs. Furthermore, although aggregation-induced emission (AIE) is typically described as the inverse phenomenon of ACQ,[35] the Hg^{2+}-induced fluorescence recovery in this system cannot be simplistically attributed to an AIE mechanism. Instead, Hg^{2+} more plausibly regulated the luminescent behavior of CuNCs through the concerted action of multiple physicochemical processes, such as ion exchange and competitive coordination, rather than relying solely on the transformation from an aggregated state to a monomeric state.

4. Conclusions

This study successfully developed a novel dual-emissive ratiometric fluorescent material, CuNCs@Eu-MOFs, by encapsulating water-soluble CuNCs into Eu-MOFs through self-assembly techniques. The material retains the optical characteristics of CuNCs and Eu^{3+}, and exhibits excellent structural and fluorescent stability in aqueous environments. CuNCs@Eu-MOFs can effectively resist interference from external environmental factors such as pH variations and prolonged storage times, ensuring the accuracy and reliability of detection results, which is particularly important in the detection of heavy metal ions, especially the highly toxic Hg^{2+}. Experimental results demonstrate that the ratiometric fluorescent sensor based on CuNCs@Eu-MOFs exhibits superior performance in Hg^{2+} detection, with broad linear range and low detection limit, enabling accurate detection of Hg^{2+} even at low concentrations. The application of this sensor in the detection of Hg^{2+} in river water and the traditional Chinese medicine *Atractylodes* has yielded good recovery rates, validating its feasibility and effectiveness in detecting Hg^{2+} in complex matrices. Furthermore, based on the multicolor fluorescence changes of CuNCs@Eu-MOFs, a portable visual fluorescent sensor has been developed. By analyzing data from smartphone color recognition apps, a correlation between Hg^{2+} concentration and the B/R value has been established, laying the foundation for the development of on-site rapid detection devices for Hg^{2+}. This study not only broadens the design concepts of ratiometric fluorescent materials but also provides theoretical support for the promotion of visual sensors in environmental monitoring, heavy metal detection and other fields.

Conflicts of interest

The authors state that there are no conflicts of interest, financial or personal, that could have affected the integrity of this work.

Data availability

Any additional data required are available from the corresponding author upon reasonable request within 30 days.

The authors confirm that the data supporting the findings of this study are available within the article and its SI. See DOI: **https://doi.org/10.1039/d5ra04013b**.

Acknowledgements

This research was funded by the Natural Science Fund Project of Hebei Province (H2022406061), Science and Technology Project of Hebei Education Department (No. 2021047), University-level Scientific Research Project in CDMC (202101) and Evaluation of Pharmaceutical Preparation and Excipients (PPE2023001).

References

1 A. D. Singh, K. Khanna, J. Kour, S. Dhiman, T. Bhardwaj, K. Devi, N. Sharma, P. Kumar, N. Kapoor, P. Sharma, P. Arora, A. Sharma and R. Bhardwaj, Critical review on

biogeochemical dynamics of mercury (Hg) and its abatement strategies, *Chemosphere*, 2023, **319**, 137917, DOI: 10.1016/j.chemosphere.2023.137917.

2 W. Li, X. Zhang, X. Hu, Y. Shi, W. Xin, N. Liang, T. Shen, J. Xiao, M. Daglia, X. Zou and J. Shi, Dual modes of fluorescence sensing and smartphone readout for sensitive and visual detection of mercury ions in Porphyra, *Anal. Chim. Acta*, 2022, **1226**, 340153, DOI: 10.1016/j.aca.2022.340153.

3 H. Guo, X. Wang, N. Wu, M. Xu, M. Wang, L. Zhang and W. Yang, In-situ synthesis of carbon dots-embedded europium metal-organic frameworks for ratiometric fluorescence detection of Hg^{2+} in aqueous environment, *Anal. Chim. Acta*, 2021, **1141**, 13–20, DOI: 10.1016/j.aca.2020.10.028.

4 K.-R. Kim, J. Oh and J.-I. Hong, A photoluminescent and electrochemiluminescent probe based on an iridium(III) complex with a boronic acid-functionalised ancillary ligand for the selective detection of mercury(II) ions, *Analyst*, 2023, **148**, 5619–5626, DOI: 10.1039/d3an01266b.

5 P. S. M. Rocha, A. S. Araújo and R. J. Cassella, Single-vial preconcentration and cold vapor generation for the determination of Hg(II) in water samples of different salinities, *Anal. Methods*, 2023, **15**, 4674–4683, DOI: 10.1039/d3ay01073b.

6 J. Gačnik, S. Lyman, S. M. Dunham-Cheatham and M. S. Gustin, Limitations and insights regarding atmospheric mercury sampling using gold, *Anal. Chim. Acta*, 2024, **1319**, 342956, DOI: 10.1016/j.aca.2024.342956.

7 H. Zou, C. Zhou, Y. Li, X. Yang, J. Wen, C. Li, S. Song and C. Sun, Speciation analysis of mercury in wild edible mushrooms by high-performance liquid chromatography hyphenated to inductively coupled plasma mass spectrometry, *Anal. Bioanal. Chem.*, 2020, **412**, 2829–2840, DOI: 10.1007/s00216-020-02515-w.

8 H. Jiao, R. Bi, F. Li, J. Chao, G. Zhang, L. Zhai, L. Hu, Z. Wang, C. Dai and B. Li, Rapid, easy and catalyst-free preparation of magnetic thiourea-based covalent organic frameworks at room temperature for enrichment and speciation of mercury with HPLC-ICP-MS, *J. Chromatogr. A*, 2024, **1717**, 464683, DOI: 10.1016/j.chroma.2024.464683.

9 X. Wang, Z. Jiang, C. Yang, S. Zhen, C. Huang and Y. Li, Facile synthesis of binary two-dimensional lanthanide metal-organic framework nanosheets for ratiometric fluorescence detection of mercury ions, *J. Hazard. Mater.*, 2022, **423**, 126978, DOI: 10.1016/j.jhazmat.2021.126978.

10 W. Meng, X. Han, R. Han, X. Zhang, X. Zeng, J. Duan and X. Luo, A highly stable electrochemical sensor with antifouling and antibacterial capabilities for mercury ion detection in seawater, *Anal. Chim. Acta*, 2024, **1309**, 342685, DOI: 10.1016/j.aca.2024.342685.

11 Y. He, Y. Wang, G. Mao, C. Liang and M. Fan, Ratiometric fluorescent nanoprobes based on carbon dots and multicolor CdTe quantum dots for multiplexed determination of heavy metal ions, *Anal. Chim. Acta*, 2022, **1191**, 339251, DOI: 10.1016/j.aca.2021.339251.

12 S. Zhang, H. Yan, H. Li, T. Xu, H. Li, C. Wang, Z. Yang, X. Jia and X. Liu, Carbon dots as specific fluorescent sensors for Hg^{2+} and glutathione imaging, *Mikrochim. Acta*, 2023, **190**, 224, DOI: 10.1007/s00604-023-05805-z.

13 N. W. Hao Guo, L. Peng, Y. Chen, Y. Liu, C. Li, H. Zhang and W. Yang, A novel ratiometric fluorescence sensor based on lanthanide-functionalized MOF for Hg^{2+} detection, *Talanta*, 2022, **250**, 123710, DOI: 10.1016/j.talanta.2022.123710.

14 Y. Lv, J. Fan, M. Zhao, R. Wu and S. Li, Recent advances in quantum dot-based fluorescence-linked immunosorbent assays, *Nanoscale*, 2023, **15**, 5560–5578, DOI: 10.1039/d2nr07247e.

15 L. Li, Q. Liu, R. Cai, Q. Ma, G. Mao, N. Zhu and S. Liu, A novel rhodamine-based fluorescent probe for high selectively determining cysteine in lysosomes, *Microchem. J.*, 2023, **187**, 108449, DOI: 10.1016/j.microc.2023.108449.

16 J. Yang, Y. Peng, S. Li, J. Mu, Z. Huang, J. Ma, Z. Shi and Q. Jia, Metal nanocluster-based hybrid nanomaterials: fabrication and application, *Coord. Chem. Rev.*, 2022, **456**, 214391, DOI: 10.1016/j.ccr.2022.214391.

17 G. Panthi and M. Park, Synthesis of metal nanoclusters and their application in Hg^{2+} ions detection: a review, *J. Hazard. Mater.*, 2022, **424**, 127565, DOI: 10.1016/j.jhazmat.2021.127565.

18 S. Li, Y. Wan, Y. Li, J. Liu, F. Pi and L. Liu, A competitive "on-off-enhanced on" AIE fluorescence switch for detecting biothiols based on Hg^{2+} ions and gold nanoclusters, *Biosensors*, 2022, **13**, 35, DOI: 10.3390/bios13010035.

19 L. Huang, P. Li, C. Lin, Y. Wu, Z. Chen and F. Fu, DNA-templated fluorescent silver nanoclusters on-off switch for specific and sensitive determination of organic mercury in seafood, *Biosens. Bioelectron.*, 2021, **183**, 113217, DOI: 10.1016/j.bios.2021.113217.

20 Y. C. Gao, C. Wang, C. X. Zhang, H. W. Li and Y. Wu, Glutathione protected bimetallic gold-platinum nanoclusters with near-infrared emission for ratiometric determination of silver ions, *Mikrochim. Acta*, 2021, **188**, 50, DOI: 10.1007/s00604-021-04710-7.

21 P. Sharma, S. Naithani, S. Layek, A. Kumar, R. Rawat, S. Kaja, A. Nag, S. Kumar and T. Goswami, Development of low-cost copper nanoclusters for highly selective "turn-on" sensing of Hg^{2+} ions, *Spectrochim. Acta, Part A*, 2023, **297**, 122697, DOI: 10.1016/j.saa.2023.122697.

22 Y. Shi, W. Li, X. Feng, L. Lin, P. Nie, J. Shi, X. Zou and Y. He, Sensing of mercury ions in Porphyra by Copper@Gold nanoclusters based ratiometric fluorescent aptasensor, *Food Chem.*, 2021, **344**, 128694, DOI: 10.1016/j.foodchem.2020.128694.

23 X. Lou, F. Yu, Z. Cao, Y. Xu, L. Yang and H. Liu, Surface motif sensitivity of dual emissive gold nanoclusters for robust ratiometric intracellular imaging, *Chem. Commun.*, 2020, **56**, 7112–7115, DOI: 10.1039/D0CC02682A.

24 M. Chen, W. Ao, J. Bai, P. Li, W. Wei, S. Pang and X. Yang, Dual-emission fluorescent nanoprobe based on Ag nanoclusters for sensitive detection of Cu(II),

Nanotechnology, 2022, **33**, 345501, DOI: **10.1088/1361-6528/ac6ff1**.

25 P. Liu, R. Hao, W. Sun, Z. Lin and T. Jing, One-pot synthesis of copper nanocluster/Tb-MOF composites for the ratiometric fluorescence detection of Cu^{2+}, *Luminescence*, 2022, **37**, 1793–1799, DOI: **10.1002/bio.4355**.

26 L. Zhang, X. Bi, H. Wang, L. Li and T. You, Loading of AuNCs with AIE effect onto cerium-based MOFs to boost fluorescence for sensitive detection of Hg^{2+}, *Talanta*, 2024, **273**, 125843, DOI: **10.1016/j.talanta.2024.125843**.

27 Y. Jiang, X. Fang, Z. Zhang, X. Guo, J. Huo, Q. Wang, Y. Liu, X. Wang and B. Ding, Composite Eu-MOF@CQDs "off & on" ratiometric luminescent probe for highly sensitive chiral detection of L-lysine and 2-methoxybenzaldehyde, *Chin. Chem. Lett.*, 2023, **34**, 108426, DOI: **10.1016/j.cclet.2023.108426**.

28 R. Xie, P. Yang, J. Liu, X. Zou, Y. Tan, X. Wang, J. Tao and P. Zhao, Lanthanide-functionalized metal-organic frameworks based ratiometric fluorescent sensor array for identification and determination of antibiotics, *Talanta*, 2021, **231**, 122366, DOI: **10.1016/j.talanta.2021.122366**.

29 X. Yang, Y. Feng, S. Zhu, Y. Luo, Y. Zhuo and Y. Dou, One-step synthesis and applications of fluorescent Cu nanoclusters stabilized by L-cysteine in aqueous solution, *Anal. Chim. Acta*, 2014, **847**, 49–54, DOI: **10.1016/j.aca.2014.08.036**.

30 Q. Zhang, X. Zhang, Y. Shu and J. Wang, Metal-organic frameworks encapsulating carbon dots enable fast speciation of mono- and divalent copper, *Anal. Chem.*, 2022, **94**, 2255–2262, DOI: **10.1016/j.aca.2014.08.036**.

31 B. Xu, H. Guo, S. Wang, Y. Li, H. Zhang and C. Liu, Solvothermal synthesis of luminescent Eu(BTC)(H_2O)DMF hierarchical architectures, *CrystEngComm*, 2012, **14**, 2914–2919, DOI: **10.1039/C2CE06537A**.

32 Z. Li, L. Chen, J. Deng, J. Zhang, C. Qiao, M. Yang, G. Xu, X. Luo, D. Huo and C. Hou, Eu-MOF based fluorescence probe for ratiometric and visualization detection of Cu^{2+}, *Spectrochim. Acta, Part A*, 2024, **304**, 123367, DOI: **10.1016/j.saa.2023.123367**.

33 R. Zhang, L. Zhu and B. Yue, A new microporous lanthanide metal-organic framework with a wide range of pH linear response, *Molecules*, 2022, **27**, 8696, DOI: **10.3390/molecules27248696**.

34 X. Zhou, X. Wang and L. Shang, Ratiometric fluorescence and visual sensing of ATP based on gold nanocluster-encapsulated metal-organic framework with a smartphone, *Chin. Chem. Lett.*, 2023, **34**, 108093, DOI: **10.1016/j.cclet.2023.108093**.

35 H. Yao, S. Liu, Z. Xing, Y. Miao, Z. Song, G. Li and J. Huang, Thionation toward high-contrast ACQ-DIE probes by reprogramming the aqueous segregation behavior: enlightenment from a sulfur-substituted G-quadruplex ligand, *Anal. Chem.*, 2022, **94**, 15231–1523, DOI: **10.1021/acs.analchem.2c03948**.